



REVIEW

Recent advances in the 3D kinematic Babcock–Leighton solar dynamo modeling

GOPAL HAZRA 

School of Physics, Trinity College Dublin, Dublin 2, Ireland.
E-mail: gopal.hazra@tcd.ie

MS received 20 August 2020; accepted 3 February 2021

Abstract. In this review, we explain recent progress made in the Babcock–Leighton dynamo models for the Sun, which have been most successful to explain various properties of the solar cycle. In general, these models are two-dimensional (2D) axisymmetric and the mean-field dynamo equations are solved in the meridional plane of the Sun. Various physical processes (e.g., magnetic buoyancy and Babcock–Leighton mechanism) involved in these models are inherently three-dimensional (3D) processes and could not be modeled properly in a 2D framework. After pointing out limitations of 2D models (e.g., mean-field Babcock–Leighton dynamo models and surface flux transport models), we describe recently developed next-generation 3D dynamo models that implement a more sophisticated flux emergence algorithm of buoyant flux tube rise through the convection zone and capture the Babcock–Leighton process more realistically than previous 2D models. The detailed results from these 3D dynamo models including surface flux transport counterparts are presented. We explain the cycle irregularities that are reproduced in 3D dynamo models by introducing scattering around the tilt angle only. Some results by assimilating observed photospheric convective velocity fields into the 3D models are also discussed, pointing out the wide opportunity that these 3D models hold to deliver.

Keywords. Sun: magnetic field—Sun: interior—Sun: dynamo.

1. Introduction

Since 1955 after Eugene Parker’s first fundamental idea (Parker 1955) on the origin of the solar magnetic cycle, it is almost more than half a century, and still, we do not understand the origin of the solar magnetic cycle very well. Understanding the solar magnetic cycle is very important not only because it provides us a great opportunity to test our existing theory of plasma physics but also it has utmost societal importance. The violent solar disturbances (e.g., solar flares and coronal mass ejections) that are driven by the magnetic field of the Sun have a strong dependence on the solar magnetic cycle and can affect the space environment tremendously.

The space environment is a complex system where the occurrence of the solar activity manifestations propagating through the interplanetary space interacts with the terrestrial magnetosphere, and generates

geomagnetic disturbances, geomagnetic storms, and aurora. The magnetic field generated by the dynamo action in the solar convection zone (SCZ) extends in the solar atmosphere and gets transported outward to the interplanetary space with the solar plasma mostly in the form of solar wind. This continuous magnetized plasma flow in the interplanetary medium interacts with the planetary magnetic field distorting their planetary magnetospheres. Besides the background solar wind, the solar activity transients, e.g., solar flares and coronal mass ejections also play a major role in driving large disturbances in space weather, such as geomagnetic storms, shock waves, and energetic particle events (Gopalswamy *et al.* 2004; Manoharan *et al.* 2004). The solar magnetic cycle affects the occurrence of transient events (Yashiro *et al.* 2004; Robbrecht *et al.* 2009; Winter *et al.* 2016) and the solar wind speed (Tokumaru *et al.* 2010), which eventually disrupts the space weather. The total

solar irradiation which varies with the solar cycle (Wu *et al.* 2018) is also a natural driver for climates in the solar system planets. Hence, a study of the solar magnetic cycle gives us an understanding of the major driving forces of space weather. Apart from the space weather, understanding the solar magnetic cycle gives us insights to understand the magnetic cycle of other solar-type stars (Karak *et al.* 2014a; Hazra *et al.* 2019) and its effect on the atmosphere of their exoplanets (Hazra *et al.* 2020).

Soon after the discovery of a magnetic field in the sunspot regions (Hale 1909), it was realized that the solar cycle or sunspot cycle is nothing but the magnetic cycle of the Sun. Efforts had been started to understand why the solar magnetic field behaves in a particular fashion with a cyclic period of 11 years. The non-linear interaction between turbulent plasma motion and the magnetic field inside the SCZ is responsible for the amplification of the magnetic field. This non-linear interaction can be understood by solving a set of magnetohydrodynamic (MHD) equations that govern the behavior of plasma and magnetic fields as given below:

$$\frac{\partial \mathbf{v}}{\partial t} + (\mathbf{v} \cdot \nabla) \mathbf{v} = \mathbf{F} - \frac{1}{\rho} \nabla p + \frac{1}{\rho c} \mathbf{j} \times \mathbf{B} + \nu \nabla^2 \mathbf{v}, \quad (1)$$

$$\frac{\partial \mathbf{B}}{\partial t} = \nabla \times (\mathbf{v} \times \mathbf{B}) + \eta \nabla^2 \mathbf{B}, \quad (2)$$

where \mathbf{v} , \mathbf{B} , ν , and η are the velocity, magnetic field, viscosity, and magnetic diffusivity, respectively. F represents the gravitational force. Other terms are as usual. Whereas the fundamental equations are well established, one of the major challenges for developing a solar dynamo model is to handle the turbulent convective motions properly inside the SCZ. The turbulent stresses in the convection zone (CZ) drive the large-scale plasma flows such as differential rotation and meridional circulation, which are very crucial for the operation of the solar dynamo. Hence, modeling turbulence in a proper way is very important to understand large-scale flows and solar dynamo theory.

Historically, the mean-field approach of turbulence played a major role in the development of the dynamo theory. In the mean-field approach, velocity field and magnetic field are split into two parts, mean and fluctuating parts:

$$\mathbf{v} = \overline{\mathbf{v}} + \mathbf{v}', \quad \mathbf{B} = \overline{\mathbf{B}} + \mathbf{B}', \quad (3)$$

where overline indicates the mean quantities and prime denotes the fluctuation from the mean. By

substituting Equation (3) in the magnetic induction Equation (2), we get

$$\frac{\partial \mathbf{B}}{\partial t} = \nabla \times (\overline{\mathbf{v}} \times \overline{\mathbf{B}}) + \nabla \times \boldsymbol{\xi} + \eta \nabla^2 \mathbf{B}, \quad (4)$$

where $\boldsymbol{\xi} = \overline{\mathbf{v}' \times \mathbf{B}'}$ is the mean electromotive force (EMF) that sustains the dynamo action in the Sun. For homogeneous isotropic turbulence, the mean EMF can be written as

$$\boldsymbol{\xi} = \alpha \overline{\mathbf{B}} - \beta \nabla \times \overline{\mathbf{B}}. \quad (5)$$

Here α represents the classical helical α -effect and β represents the turbulent diffusivity (see Choudhuri (1998) for details).

At present, the most promising framework to explain the properties of the solar magnetic field is the Babcock–Leighton (BL)/flux transport dynamo (FTD) model (Choudhuri *et al.* 1995; Durney 1995, 1997; Dikpati & Charbonneau 1999; Chatterjee *et al.* 2004; Hazra *et al.* 2014; Karak *et al.* 2014b). These models are a class of mean-field dynamo models where the BL α effect is considered instead of the classical helical α effect, and meridional flow plays a very important role. The mean solar magnetic field is generally assumed to be axisymmetric in these models and can be decomposed into two parts, namely the toroidal and poloidal components. Parker (1955) first suggested that the solar magnetic cycle is a result of oscillation between the toroidal field and the poloidal field, and the toroidal and poloidal fields sustain each other through a cyclic feedback process. For the Sun, as the equator rotates faster than the pole, the differential rotation stretches the poloidal field and generates the toroidal field. When the toroidal field becomes magnetically buoyant, it rises and pierces the surface to create the sunspots. The bipolar sunspots always have an angle in between them (tilt angle) with respect to the equatorial line because of the Coriolis force that acted on the toroidal field while it rises through the CZ due to magnetic buoyancy (D’Silva & Choudhuri 1993). Since the Coriolis force increases with increasing latitudes, the tilt angle also increases as sunspots erupt at the higher latitudes, which is first observed by Joy and known as Joy’s law (Hale *et al.* 1919). Also, sunspots are the regions of the strong magnetic field and they diffuse. As a result, the leading polarity sunspots that are near the equator cancel with opposite polarity sunspots from the opposite hemisphere. The trailing polarity sunspots from each hemisphere advect to the polar region and generate the large-scale poloidal field. This whole

mechanism is called the BL mechanism (Babcock 1961; Leighton 1969). This mechanism plays a very crucial role in the BL dynamo model by converting the toroidal field to the poloidal field. Once the large-scale poloidal field is generated on the surface of the Sun, it is advected to the bottom of the CZ by the meridional circulation or the turbulent diffusion, depending upon which one has the faster time scale. As the BL mechanism needs the involvement of the longitudinal coordinate over the surface of the Sun and most of the BL/FTD model follows a two-dimensional (2D) axisymmetric formulation in which the magnetic induction equation is solved in the meridional plane of the Sun, a parametric approach has been widely used to capture the BL mechanism in the 2D BL models.

The BL mechanism is observationally very well supported. Kitchatinov & Olemskoy (2011) calculated the global poloidal field by multiplying tilt angle and the magnetic field strength of active regions for an individual cycle, which is correlated with the strength at the minimum of that following cycle. Dasi-Espuig *et al.* (2010) also found a significant correlation between the product of the cycle's averaged tilt angle and the strength of the same cycle with the strength of the next cycle supporting the BL mechanism.

There is another class of models that treat the BL mechanism more realistically than the parametric approach used in the 2D axisymmetric BL dynamo models. These are called surface flux transport (SFT) models (Wang *et al.* 1989a, b; Baumann *et al.* 2004; Jiang *et al.* 2014a). Note that these are not dynamo models rather they only consider the evolution of the radial field on the surface of the Sun. In these models, sunspots are directly incorporated and the decay of sunspots due to turbulent diffusivity and corresponding advection of fields to the pole by meridional circulation is modeled by solving the radial part of the magnetic induction equation on the surface (latitude–longitude plane) of the Sun. They capture the realism of the BL mechanism in great detail but they have their own limitations.

In both types of models (BL dynamo models and SFT models), mean flows (e.g., meridional flow and differential rotation) play a very important role. We have an overwhelming amount of data from helioseismology for mean flows (Thompson *et al.* 1996; Antia *et al.* 2008). For SFT models, the required surface information of the mean flows is well constrained. However, for the BL dynamo model, we need information about the mean flows inside the whole CZ, in which the differential rotation is well mapped (Antia *et al.* 1998; Schou *et al.* 1998) but the

exact nature of meridional circulation is still an active field of research. In most of the BL dynamo model, a single-cell meridional circulation encompassing the whole CZ with a poleward flow near the surface and an equatorward return flow near the base of the CZ is assumed. The poleward flow near surface is observed by helioseismology but detecting the equatorward return flow is an extremely difficult task because of very high noise in the helioseismology data near the bottom of the CZ. However, recently, Gizon *et al.* (2020) found a single-cell meridional circulation with an equatorward return flow in each hemisphere of the Sun. Also, some of the numerical simulations find the equatorward return flow due to angular momentum balance with the solar-like differential rotation (Passos *et al.* 2015).

Most 2D BL dynamo models are successful in explaining various properties and irregularities of the solar magnetic cycle. However, some of the solar magnetic features, e.g., active longitudes are beyond the scope of these axisymmetric 2D dynamo models. Active longitudes are the longitudinal locations of the Sun where the solar magnetic activity is strong. The sunspot data obtained from various observatory show the evidence of active longitudes on the Sun very clearly (Berdyugina 2005; Dikpati & Gilman 2005; Usoskin *et al.* 2005; Mandal *et al.* 2017). Also, recently, a strong quasi-annual variability in the number of flares and CME driven by the surges of magnetism from the activity bands is observed (McIntosh *et al.* 2015; Dikpati *et al.* 2018). A three-dimensional (3D) dynamo model would be extremely helpful to reproduce these nonaxisymmetric active longitudes' features and short-term variability in the solar cycle.

Apart from well-observed magnetic features, some of the processes involved in the dynamo model are not well constrained from observations. The toroidal field generation mechanism from the poloidal field by differential rotation is well constrained from helioseismology. However, the flux emergence due to magnetic buoyancy and creation of sunspots—this whole process is an inherently 3D process and could not be modeled properly in 2D. Also, due to the lack of azimuthal information in 2D models, the realism of the BL process cannot be captured as it is done in SFT models. However, the SFT models have their own limitations for not considering subsurface processes (e.g., subduction of the magnetic field by meridional circulation in the polar regions) and the 3D vectorial nature of the magnetic field. Therefore, the development of 3D dynamo models will help in capturing the 3D processes involved in the dynamo model more

realistically and build a bridge between 2D BL dynamo models and SFT models. Also, it will help us with new opportunities to assimilate the observed photospheric data to probe the interior of the SCZ.

This review is structured as follows. In the next section, we will briefly describe the advantages and disadvantages of the 2D models including SFT models. The formulation of next-generation 3D dynamo models based on newly developed flux emergence algorithms and some results are given in Section 3. The advantage of 3D models compared to the 2D models in the light of the build up of the polar field is discussed in Section 4. In Section 5, we discussed how irregular properties of the solar cycle can be studied by including a more realistic treatment of tilt angle scatters around Joy's law. The opportunity of observed data assimilation in the 3D models and some enlightening results including those data are presented in Section 6. Finally, in Section 7, we summarize and conclude all results from 3D models indicating the tremendous possibility that these models have to emerge as the next-generation dynamo models.

2. 2D models

2.1 2D axisymmetric BL/FTD models

The mean axisymmetric magnetic field of the Sun can be written as

$$\mathbf{B} = B_\phi \hat{\phi} + \nabla \times A \hat{\phi}, \quad (6)$$

where B_ϕ is the toroidal field and $A \hat{\phi}$ is the magnetic vector potential, curl of which gives rise to the poloidal field. The toroidal and poloidal field evolution equations are given below:

$$\frac{\partial A}{\partial t} + \frac{1}{s} (\mathbf{v} \cdot \nabla)(sA) = \eta_p \left(\nabla^2 - \frac{1}{s^2} \right) A + S(r, \theta, t), \quad (7)$$

$$\frac{\partial B}{\partial t} + \frac{1}{r} \left[\frac{\partial}{\partial r} (rv_r B) + \frac{\partial}{\partial \theta} (v_\theta B) \right] = \eta_t \left(\nabla^2 - \frac{1}{s^2} \right) B + s(B_p \cdot \nabla) \Omega + \frac{1}{r} \frac{d\eta_t}{dr} \frac{\partial (rB)}{\partial r}. \quad (8)$$

Here B_p is the poloidal field, $s = r \sin \theta$, and other terms are as in usual notation. $S(r, \theta)$ is the source function that incorporates the flux emergence through the CZ and subsequent BL process.

In most of the dynamo models, observationally motivated various analytical profiles of the differential

rotation (Ω) and meridional flow (v_r, v_θ) are used, which are very close to the helioseismology findings. A particular profile of differential rotation and meridional flow is shown in Figure 1. In general, a single-cell meridional circulation is used. Although the equatorward return flow near the bottom of the CZ for the single-cell meridional circulation is extremely difficult to observe by helioseismology, it is needed in order to fulfill the mass conservation. However, recently Gizon *et al.* (2020) found an equatorward flow near the bottom of the CZ supporting a single-cell meridional circulation. This equatorward flow plays a very important role in advecting the toroidal field toward the equator against the poleward dynamo wave (Yoshimura 1975) explaining the equatorward migration of the sunspots. Even in the case of multi-cell meridional circulations inside the SCZ, this equatorward return flow near the bottom of the CZ is important for the dynamo to work (Hazra *et al.* 2014).

The parametric approach of modeling magnetic buoyancy and BL process widely varies across different 2D dynamo models. It can be classified into two specific approaches, one local buoyancy and another one as nonlocal buoyancy. In the local buoyancy treatment, the toroidal field is depleted from the bottom of the CZ once it is more than a critical value and placed on the surface to account for the poloidal field generation. The depleted toroidal field is usually multiplied by an α -parameter, which is confined near the surface layers. In nonlocal buoyancy treatment, the toroidal field at the bottom of the CZ is directly

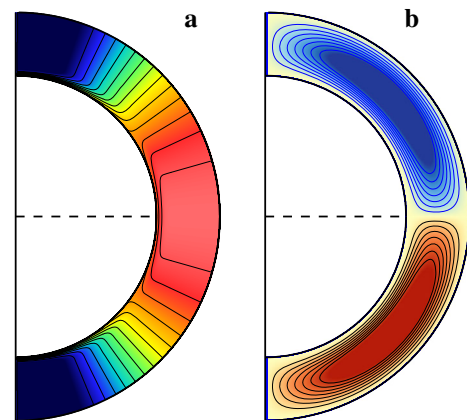


Figure 1. (a) Differential rotation profile. Color scale represents differential rotation with value 350–480 nHz from blue to red and (b) the meridional flow streamlines. Blue contours show the poleward flow at the surface and an equatorward flow at the bottom of the CZ in the northern hemisphere and red contours show the same in the southern hemisphere. From Hazra *et al.* (2017).

multiplied with the α -parameter on the surface to generate the poloidal field. For a detailed discussion about the treatment of magnetic buoyancy see Choudhuri & Hazra (2016). In general, both the treatments of the magnetic buoyancy reproduce the basic features (e.g., 11-year periodicity, equatorward migration of sunspots, and polarity reversal) of the observed solar cycle quite well. However, depending upon how we treat the magnetic buoyancy in 2D models, many irregularities of the solar cycle (e.g., Waldmeier effect and correlation of decay rate with next cycle amplitudes) may or may not be reproduced. Also, Muñoz-Jaramillo *et al.* (2010) pointed out that α -parameterization does not correctly depict the relation between the speed of surface meridional flow and strength of the polar field, rather another formalism called Durney’s double-ring algorithm (Durney 1995, 1997) catches the intuitive process of BL mechanism more physically. Given that many parametric formalisms of magnetic buoyancy and the BL process in 2D models lead to varied results, the next step would be to model the flux emergence due to magnetic buoyancy and subsequent sunspots decay due to the BL process using a 3D framework (Yeates & Muñoz-Jaramillo 2013; Miesch & Dikpati 2014; Miesch & Teweldebirhan 2016; Hazra *et al.* 2017; Hazra & Miesch 2018; Karak & Miesch 2018).

2.2 SFT models

The visible part of the BL process on the surface, i.e., the dispersion and migration of the sunspot fields after sunspots emerge are well captured in the SFT model. However, unlike BL dynamo models, it only solves the radial component of the magnetic induction equation on the surface of the Sun in the latitude–longitude plane. The radial component of the magnetic induction equation on the surface of the Sun (at $r = R_\odot$) is given below:

$$\begin{aligned} \frac{\partial B_r}{\partial t} = & -\frac{1}{R_\odot \sin \theta} \frac{\partial}{\partial \phi} (u B_r) - \frac{1}{R_\odot \sin \theta} \frac{\partial}{\partial \theta} (v B_r \sin \theta) \\ & + \eta_H \left[\frac{1}{R_\odot^2 \sin \theta} \frac{\partial}{\partial \theta} \left(\sin \theta \frac{\partial B_r}{\partial \theta} \right) + \frac{1}{R_\odot^2 \sin^2 \theta} \frac{\partial^2 B_r}{\partial \phi^2} \right] \\ & + S(\theta, \phi, t) + D(B_r). \end{aligned} \quad (9)$$

The radial component of the magnetic field (B_r) has been used as a passive scalar here that can be mixed and advected to the pole under the effective action of differential rotation, i.e., the velocity in the longitudinal direction (u), latitudinal meridional flow (v), and turbulent diffusion (η_H). $S(\theta, \phi, t)$ incorporates the

new fluxes that emerge from the surface below. $D(B_r)$ is the term that takes care of the decay of the magnetic field due to radial diffusion. Historically, this model plays a tremendous role in understanding the BL process and subsequent build up of the polar field. In this model, one can study in detail that how individual sunspot pair contributes to the build up of the polar field, and how the latitudinal position of the sunspots and their tilt angle distribution are going to affect the strength of the polar field. The main limitation of the model is not accounting for many important physics by ignoring the vectorial nature of the magnetic field and by not incorporating the subsurface processes. There are some studies that show that the subduction of the poloidal field by the meridional flow sinking underneath the solar surface plays a very important role in the dynamics of the magnetic field (Dikpati & Choudhuri 1994, 1995; Choudhuri & Dikpati 1999). Since these processes cannot be incorporated in 2D SFT models, the advected radial magnetic flux near the polar region tends to get piled up and it can only be neutralized by the opposite polarity flux advected there. Therefore, if the additional flux of opposite polarity is not advected to the polar regions, the polar field may reach an asymptotic value (see Figure 6 of Jiang *et al.* 2014a). One may get a secular drift of the polar field while modeling several cycles if the flux of the succeeding cycle is unable to properly neutralize the polar flux of the preceding cycle. Baumann *et al.* (2004, 2006) proposed a way of fixing this problem by adding an *ad hoc* decay term corresponding to the radial diffusion, which is not included in the SFT model. Hence, although SFT models played a very important role in elucidating the BL process, it has some inherent limitations that it cannot handle the dynamics of the magnetic field in the polar regions appropriately.

The next step would be to develop the 3D kinematic BL dynamo models where the fluid motions are still provided and the evolution of the magnetic field would be in 3D. These models can incorporate the attractive features of the 2D BL dynamo models and SFT models while being free from the limitations of both of the models.

3. 3D kinematic dynamo models

3D dynamo models are the next-generation dynamo models that implement the BL process with high observational fidelity and treat magnetic flux emergence through the SCZ much more realistically than

2D dynamo models. In these models, the total non-axisymmetric magnetic field of the Sun is considered and their evolution is studied by solving the magnetic induction equation in a 3D rotating spherical shell with a radius ranging from $r = 0.69 R_{\odot}$ to $r = R_{\odot}$ as given below:

$$\frac{\partial \mathbf{B}}{\partial t} = \nabla \times (\mathbf{v} \times \mathbf{B} - \eta \nabla \times \mathbf{B}) + S(r, \theta, B, t), \quad (10)$$

where $\mathbf{B}(r, \theta, \phi, t)$ is written in terms of toroidal and poloidal magnetic potentials A and C such that

$$\mathbf{B} = \nabla \times (A\hat{r}) + \nabla \times \nabla \times (C\hat{r}).$$

η is the magnetic diffusivity inside the SCZ and v is the mean flow. In most of the cases, a radial field at the surface and a conducting lower boundary have been used as boundary conditions for solving Equation (10). Although the magnetic field is in 3D, the velocity fields are still axisymmetric in general. However, Hazra & Miesch (2018) considered the effect of nonaxisymmetric velocity fields to study the BL process. The source term $S(r, \theta, t)$ incorporates the BL process and magnetic flux emergence through the SCZ. The inherent 3D nonaxisymmetric features of flux emergence due to magnetic buoyancy is now modeled more realistically in 3D models. Different treatments on every aspect of flux emergence and BL processes in the 3D framework are discussed in the next subsections.

3.1 Flux emergence

First time in a 3D framework, Yeates & Muñoz-Jaramillo (2013) modeled the full process of 3D

emergence of flux tube considering its interaction with convective flows while rising through the SCZ. Their procedure is really unique in the way that it incorporates key features of emerging flux tubes, as suggested by the thin-flux tube and anelastic MHD simulations, and allows the flux emergence in a more consistent way than artificial flux deposition on the surface of the Sun. This treatment of flux emergence in the dynamo framework would enhance our understanding of the emergence and decay of sunspots as a source for creating the poloidal field from the toroidal field. In Figure 2, the emergence of two isolated flux tubes at two different latitudes (0° and 30°) are shown. It is clear from the simulation that the rotational shear of the emerging flux tube leads to the relative movement of the flux tube with respect to its roots, which is very important for the magnetic configuration near the eruption site.

Another method that has been developed to incorporate flux emergence and the corresponding creation of sunspots is called the ‘‘Spotmaker’’ algorithm (Miesch & Dikpati 2014; Miesch & Toweldibirhan 2016; Hazra *et al.* 2017; Karak & Miesch 2018). This method is different from the flux emergence procedure adopted in Yeates & Muñoz-Jaramillo (2013). In the Spotmaker algorithm, the spots are placed on the surface of the Sun based on dynamo-generated toroidal field near the base of the CZ. In this method, the time required for flux to travel through the CZ is neglected with respect to the time scale of the solar cycle.

As a first step, the spot-producing toroidal field is calculated at the tachocline by averaging a toroidal field over the radius from $r = 0.70 R_{\odot}$ to $r = 0.71 R_{\odot}$. Then the bipolar spot is placed once the averaged

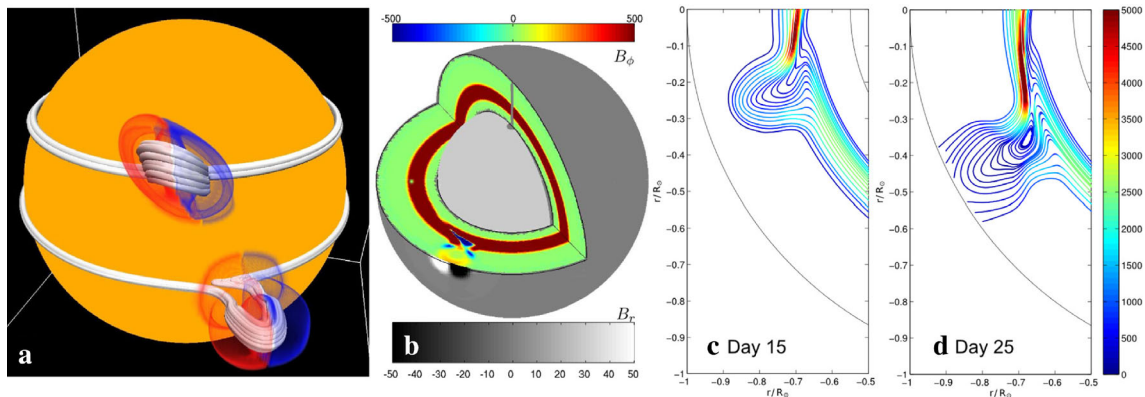


Figure 2. This figure is taken from Yeates & Munoz-Jaramillo (2013) showing a single flux tube emergence on day 25 at two different latitudes (a) at 30° N and 0° latitudes. Red and blue on the surface show positive and negative polarity B_r , respectively. (b) Colored contours show a cut of B_{ϕ} inside the CZ and contours on the surface show B_r (on day 25). The magnetic field lines in the equatorial plane on days 15 and 25 are shown in (c) and (d). All color bars are in units of Gauss.

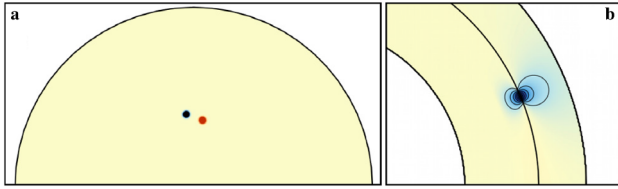


Figure 3. Structure of a typical spot pair produced by the “Spotmaker” algorithm following Joy’s law tilt. (a) Orthogonal projection of B_r at the solar surface associated with two spots at the mid-latitude. Red and blue show positive and negative polarity of sunspots, respectively. (b) The poloidal field associated with the spot pairs. The potential field used for a subsurface structure extended up to $0.95 R_\odot$. This figure is taken from Miesch & Dikpati (2014).

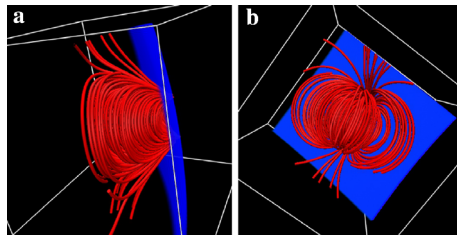


Figure 4. The detailed subsurface structure of magnetic field lines in a sunspot pair is shown from Miesch & Teweldebirhan (2016). The volume rendering shows magnetic field lines (red contours) below the solar surface at two different vantage points (a) east of the sunspot pair looking west and (b) underneath the sunspot pair looking up. The surface of the Sun is shown by the blue surface.

toroidal field near the tachocline exceeds a threshold value B_t as shown in Figure 3(a). The corresponding potential field approximation of the placed sunspot is also shown in Figure 3(b). The placement of a spot pair on the surface in latitude and longitude is decided by the location where the averaged toroidal field crosses the threshold value. However, after emergence, the spots are not connected to their parent flux tubes. A potential field extrapolation below the surface of each spot pair is used for the subsurface structure. The subsurface structure of each spot is shown in Figure 4(a) and (b).

After deciding the locations of the spot pair, the timing for sunspots appearance is determined by a time delay probability density function motivated from the observed sunspots data. For example, if a sunspot pair appears at time t_0 , then the timing of the next emergence event will be at $t_1 = t_0 + \Delta_n$, where Δ_n is chosen randomly based on the time delay probability distribution function $P(\Delta)$ (Miesch & Teweldebirhan 2016). Once the sunspot pairs are placed on the surface of the sun based on the

locations and timing determined by the toroidal field and time delay probability distribution function (PDF), their subsequent evolution due to differential rotation, meridional circulation, and turbulent diffusion generates the poloidal field naturally via the BL mechanism. The Spotmaker algorithm captures much better the sunspots properties after emergence, i.e., the late phase of the flux emergence on the surface while the procedure adopted in Yeates & Muñoz-Jaramillo (2013) captures the early phase of the flux emergence better.

Recently, Kumar *et al.* (2019) have employed the dynamical flux emergence by considering upward vortical flows and subsequent evolution of the spots to create the poloidal field. Unlike Yeates & Muñoz-Jaramillo (2013), they are able to obtain a self-excited dynamo but this dynamic flux emergence algorithm gives rise to the overlapping sunspot distribution near the minima. A comparative study of different flux emergence algorithms to explain various irregular properties might be very helpful to constrain the exact flux emergence method.

3.2 Dynamo quenching and BL process

One of the main issues related to the kinematic approach of dynamo modeling is not accounting for the Lorentz force feedback on the mean flows. Presumably, for the Sun, the kinematic approach is not at all a bad approximation because the observed torsional oscillation, i.e., the cyclic variation of the differential rotation is not very significant (Antia & Basu 2000; Chakraborty *et al.* 2009) and the results obtained from these models are quite in good agreement with the observations. However, in the kinematic framework, the dynamo needs to be quenched for a given velocity field to suppress its unlimited growth. In the Spotmaker algorithm, the flux being deposited on spot pairs is suppressed by a quenching factor:

$$\Phi_s = 2\Phi_0 \frac{|B(\theta_s, \phi_s, t)|}{B_q} \frac{10^{23}}{1 + (B(\theta, \phi)/B_q)^2} \text{Mx}, \quad (11)$$

where B is the toroidal field averaged over the tachocline and B_q is the quenching field strength usually assumed to be 10^5 G. The Φ_0 factor is the amplification factor, which can be adjusted to make dynamo action to be supercritical. If we choose $\phi_0 \sim 1$, which will give a flux of 10^{23} Mx in the strongest active region closed to the observations with

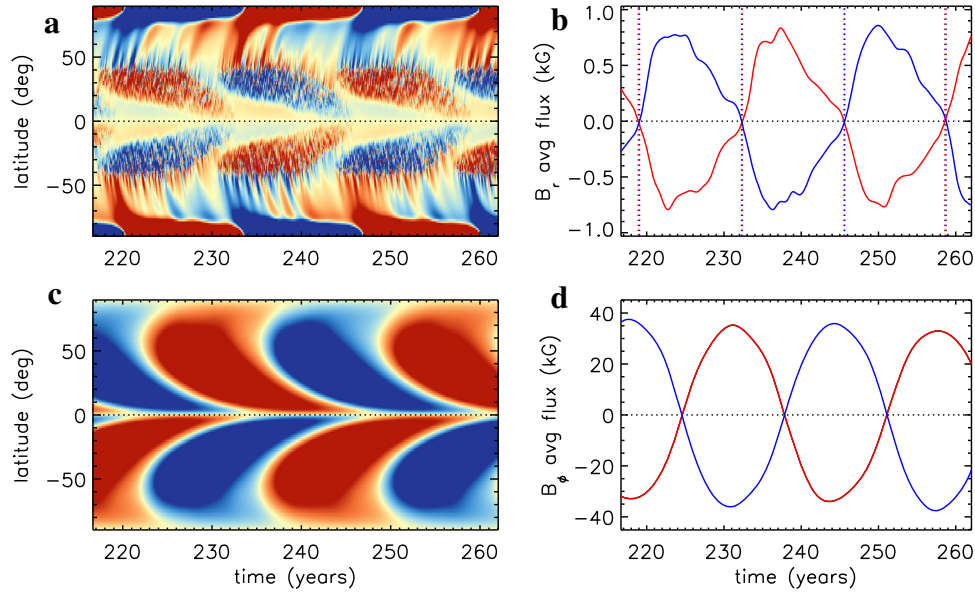


Figure 5. Magnetic cycles from a standard STABLE simulation taken from Hazra & Miesch (2018). (a) The azimuthal averaged B_r is shown as a function of time and latitudes, highlighting three cycles. Red and blue show positive and negative polarity, respectively. The color scale is set from -200 G (blue) to $+200$ G (red). (b) Mean polar field, i.e., the averaged radial field over latitudes poleward of $\pm 88^\circ$ for the same three cycles is shown. Polar field reversals are shown using the dotted lines. Blue and red correspond to the northern and southern hemispheres, respectively. (c) Time–latitude plot of the azimuthal averaged mean toroidal field \hat{B}_ϕ at $r = 0.7 R_\odot$ (bottom of the CZ). The color scale saturates at ± 50 kG, with red and blue denoting eastward and westward fields, respectively. (d) Evolution of mean toroidal flux near the base of the CZ averaged over the northern (blue) and southern (red) hemispheres for the same three cycles.

the subsurface toroidal field strength equivalent to the quenching field strength.

Another very physical way to incorporate dynamo quenching is by introducing a quenching factor in the tilt angle between the bipolar magnetic regions (BMRs). As the strongest flux tubes get less affected by the Coriolis force while rising fast through the SCZ, we expect the tilt angle to be quenched when the cycle strength is strong. Karak & Miesch (2017) used the tilt angle quenching as the dynamo saturation mechanism and were able to get a self-sustained dynamo solution.

3.3 Evolution of dynamo-generated fields

We present results from the self-sustained 3D kinematic dynamo models called surface flux transport and Babcock–Leighton (STABLE) dynamo model here, which have mostly been presented in Miesch & Dikpati (2014), Miesch & Teweldebirhan (2016), Hazra *et al.* (2017), Karak & Miesch (2017), and Hazra & Miesch (2018). The butterfly diagram is mostly considered as the signature of the cyclic properties of the solar cycle. In Figure 5(a) and (c),

the butterfly diagram, i.e., the time latitude diagram of azimuthal averaged toroidal and radial fields are shown at $r = 0.71 R_\odot$ and $r = R_\odot$, respectively. The butterfly diagrams show a cyclic behavior in both toroidal and radial fields with a nearly 13-year periodicity. The fine tuning of meridional flow speed or turbulent diffusion can give us exactly the 11-year period of the solar cycle but we want to explore the overall properties of the solar magnetic activity. The equatorward propagation of the sunspot field is clear from the radial field evolution diagram (Figure 5a). The sunspot producing field, i.e., the toroidal field also shows an equator migration with time (Figure 5c) presumably due to the equatorward meridional circulation near the bottom of the CZ. Since there is no physical sunspot number in most of the previous 2D models, the toroidal field at the bottom of the CZ is considered as a proxy of the sunspot number. However, for the 3D model, we have physical sunspots on the surface that contributes to the polar field. The disintegration and migration of the sunspot field due to meridional circulation, differential rotation, and turbulent diffusion give rise to a poleward migration of trailing flux that reverses the polar field according to the BL mechanism (see Figure 5a).

In Figure 5(b) and (d), the evolution of polar flux and averaged toroidal flux over each hemisphere is shown. Polar flux is calculated by averaging a radial field on the polar region above $\pm 85^\circ$ latitudes, while toroidal flux is calculated over the whole CZ in each hemisphere. The opposite phase difference between the evolution of toroidal flux and polar flux makes it clear that the polar field reaches a minimum value while the toroidal field is maximum, i.e., during the solar maximum in accordance with the observation.

The solar active longitudes could not be explained from our 3D model because the longitudinal information of sunspot formation is still random in our model. The dynamo-generated field near the tachocline is randomly put on the surface to form sunspots when it crosses a particular threshold value (see Section 3.1 for details). A promising theory to explain these active longitudes and their time variation involves hydrodynamic (HD) and MHD Rossby waves inside the Sun and has been developed over the past 20 years (see, e.g., Dikpati & McIntosh (2020) and references therein). The interaction of Rossby waves with differential rotation and toroidal fields generates tachocline nonlinear oscillations (TNOs), which are very robust features of the tachocline in MHD shallow water models and are demonstrated to be responsible for both solar active longitudes and short-term solar seasonal/sub-seasonal variability (Dikpati & Gilman 2005; McIntosh *et al.* 2015; Dikpati *et al.* 2018). The inclusion of the TNOs in the 3D model while modeling the flux emergence from the tachocline to the surface would be very crucial in modeling active longitudes and the solar seasonal/sub-seasonal variability. The 3D dynamo models are capable of reproducing most of the aspects of the solar magnetic field with a very good promise to include many observational data for a greater understanding of solar magnetic activity as we explain in the next sections.

4. Behavior of SFT in the 3D dynamo model

The addition of an extra azimuthal dimension in the 3D models allows us to investigate the behavior of flux transport on the surface of the Sun. Hence, one of the main aspects that we can address after constructing a self-excited 3D dynamo model is how an individual sunspot pair contributes to the building up of the polar field and whether our understanding gained from the 3D models necessitates the revision of some insights

gained from 2D SFT models. In order to do that an individual sunspot pair on each hemisphere is placed at a particular latitude and let them evolve under the axisymmetric mean flows and turbulent diffusion. Hazra *et al.* (2017) explored a few cases by putting a single sunspot pair in the northern hemisphere, two sunspot pairs symmetrically in two hemispheres, and two sunspot pairs in two hemispheres at two different longitudes as well (not symmetric). We discussed here only one case in detail, where two sunspot pairs are placed symmetrically in two hemispheres.

4.1 Build up of polar field from two sunspot pairs in two hemispheres

The ‘‘Spotmaker’’ algorithm (as explained in Section 3.1) is used to place two sunspot pairs symmetrically across the equator at two hemispheres at $\pm 5^\circ$ latitudes. The magnetic flux in each spot is chosen as 1×10^{22} Mx and its radius is taken to be 21.71 Mm. To make the result of our simulation more clearly visible, the radius of each sunspot is chosen somewhat larger than the actual sunspot. After placing the sunspots successfully, we allow our code to evolve the magnetic field from these sunspot pairs leading to the build up of the polar field. The snapshots of the radial magnetic field (B_r) at different times during the evolution of the magnetic field are shown in Figure 6. Figure 7 shows the evolution of the toroidal field and the poloidal field at different times after the initial placement of the sunspot pairs. As soon as a sunspot pair is placed using the ‘‘Spotmaker’’ algorithm, some toroidal field arises below the surface at once because the magnetic loop connecting two sunspots below has a toroidal component. Also, a more toroidal field is generated because of the latitudinal differential rotation in the CZ.

If the two pairs of sunspots are sufficiently close to the equator, then leading polarity sunspots from both hemispheres get canceled by diffusion across the equator. The trailing polarity sunspots are preferentially transported to the higher latitudes and get stretched by differential rotation. The meridional circulation takes almost 3 years to bring flux of B_r to produce a positive patch at the northern hemisphere and a negative patch in the southern hemisphere as shown in Figure 6. The polar magnetic patches form with the polarity of the trailing sunspots. However, a careful look at Figure 6 shows some evidence of opposite polarity of what we see in the poles at

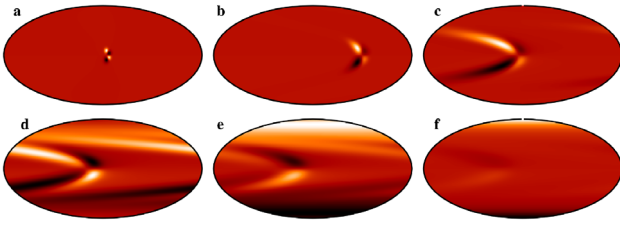


Figure 6. The evolution of radial magnetic fields on the surface of the Sun for sunspot emergence in two hemispheres at $\pm 5^\circ$ latitudes during (a) 0.025 year, (b) 0.25 year, (c) 1.02 years, (d) 2.03 years, (e) 3.05 years, and (f) 4.06 years. Here, white and black show the outward and inward going radial field, respectively. In each case, the color scale is set at \pm maximum values of the magnetic field. For example, in case (a), the color scale is set at ± 4.66 and ± 0.10 G is the color scale for (f). From Hazra *et al.* (2017).

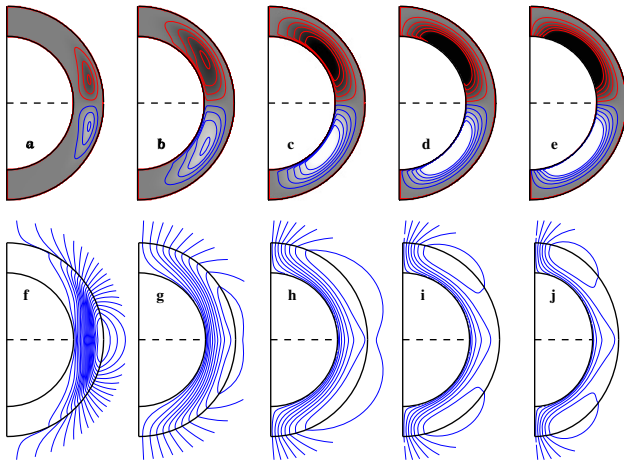


Figure 7. Snapshots of axisymmetric toroidal field lines (a)–(e) and axisymmetric poloidal field lines (f)–(j) are shown at five different times—(a), (f) = 1.02 years, (b), (g) = 3.05 years, (c), (h) = 5.08 years, (d), (i) = 7.11 years, and (e), (j) = 9.15 years. Line contours in frames (a)–(e) show \hat{B}_ϕ (azimuthal averaged) with red and blue indicating eastward and westward fields, respectively. The filled contour represents the strength of the mean toroidal fields (color scale = ± 1.5 G). The square root of poloidal magnetic potential with potential field extrapolation above the surface (up to $r = 1.25 R$) is shown in frame (f)–(j). Blue contours denote the clockwise direction of the field. Contour levels corresponding to the poloidal fields strengths of ± 0.02 G are fixed as maximum and minimum, respectively. Taken from Hazra *et al.* (2017).

mid-latitudes even two sunspots are placed symmetrically at sufficiently low latitudes in both the hemispheres. To understand the physics of what is happening, we need to focus on the poloidal field lines plot in the bottom panel of Figure 7(f)–(g). After

magnetic fluxes from the leading sunspots near the equator cancel out, we get initial poloidal field lines spanning both hemispheres. As is clear from the early stage of magnetic field evolution (Figure 7f), we have B_r only at high latitudes. In the later stage, when meridional circulation drags the poloidal field lines toward poles, eventually polar fields in two hemispheres get detached, as a result of which B_r again appears at lower latitudes having the opposite polarity of B_r at high latitudes.

In the 2D SFT model, only the fluxes from the following polarities are advected toward the poles and we eventually get polar patches that are not surrounded by the opposite polarity patches, as found in the 3D models. The outward spreading magnetic field from the polar patches by diffusion is eventually balanced by the inward advection by the meridional circulation and an asymptotic steady state is reached in the SFT model, with an asymptotic magnetic dipole that does not change with time (see Figure 6 of Jiang *et al.* 2014a). However, for the 3D case, a different scenario arises because of the 3D structure of the magnetic field. As $\nabla \cdot \mathbf{B} = 0$, $\int \mathbf{B} \cdot d\mathbf{S}$ integrated over the whole surface has to be zero at any time. This means that during any time interval, equal amounts of positive and negative magnetic fluxes need to disappear below the surface due to the subduction process. Hence, the low-latitude emergence of the B_r is due to the 3D structure of the magnetic fields. Since full vectorial nature is not considered in the SFT model, low latitudes B_r would never appear in that model. Because breakup of the poloidal field and the appearance of B_r at the low latitudes with opposite polarity, it is possible for the poloidal field to be subducted below the surface in the two hemispheres as the meridional circulation sinks downward in the polar regions. Hence, in contrast to the SFT models where polar fields have nothing to cancel them and therefore persist, the polar fields disappear after some time in the 3D model.

Next, we present results by placing two sunspot pairs symmetrically at different latitudes in the two hemispheres. The evolution of the polar field for sunspot pairs placed at different latitudes is shown in Figure 8. The sunspot pairs that are placed at high latitudes advects less path to the poles and lost less flux due to diffusion and as a result, the polar field becomes stronger for high latitudes of emergence. Eventually, the polar field disappears in all cases due to subduction by the meridional flows and diffusion. Figure 8 can be directly compared with the left panel

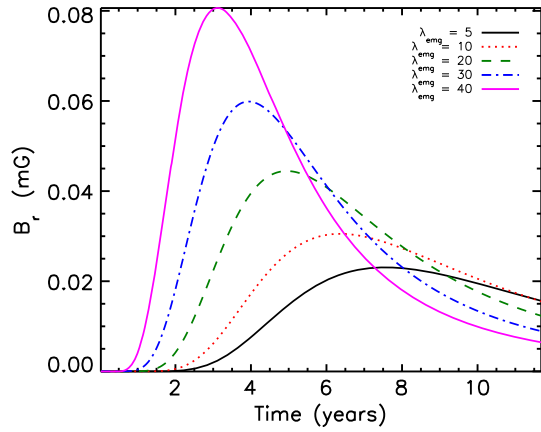


Figure 8. Time evolution of polar field for different emergence angle (λ_{emg}) of sunspot pairs in both hemispheres from Hazra *et al.* (2017). Black solid, red dotted, green dashed, blue dash-dotted, and magenta long dash-dotted lines show the polar field for the sunspot emergence at 5° , 10° , 20° , 30° , and 40° , respectively. The unit of the magnetic field is in milliGauss and time is given in years.

of Figure 6 of Jiang *et al.* (2014a) where the time evolution of axial dipole moments is shown. This comparison makes the difference between the 3D model and the SFT model completely clear. In the SFT model, the cross equator diffusion for the sunspot pairs that are put at sufficiently high latitudes is negligible and fluxes of both polarities are advected to the polar region, and eventually, the axial dipole moment becomes zero. In the case of sunspots pair placed at low latitudes in the SFT model, only the fluxes from the following polarity sunspots reach the poles and give rise to an asymptotic axial dipole. The situation becomes completely different in the 3D model. However, we see the persistence of polar fields for a longer time when the initial sunspots are placed at lower latitudes. The sunspot pairs appearing in lower latitudes is somewhat more effective in creating the poloidal field even in the 3D model. This finding is also in agreement with the results of Dasi-Espuig *et al.* (2010) who found a better correlation between the average tilt of a cycle and the strength of the next cycle if more weight is given to sunspot pairs at low latitudes while computing the average tilt.

Although the difference between the result of the SFT model and the 3D model is notable, it may be offset to some extent by including efficient downward radial pumping. Karak & Cameron (2016) have shown that downward radial pumping due to strongly stratified convection near the solar surface can suppress the upward diffusion of toroidal and poloidal fields. Hence, turbulent pumping can help to produce a

steady polar field that might persist indefinitely. The exact role of this turbulent pumping needs to be investigated thoroughly.

4.2 Contribution of anti-Hale sunspot pairs to the polar field

Since the build up of the polar field is much realistically captured in the 3D model compared to the SFT models, we now address another important question that whether the anti-Hale sunspot pairs have a large effect on the polar field in the 3D dynamo model. It is well known that some of the BMRs appear on the solar surface with wrong magnetic polarities not obeying Hale’s polarity law. While flux tubes rise through the SCZ, it gets affected by the action of turbulence (Longcope & Choudhuri 2002; Weber *et al.* 2011). As a result, we see a spread of tilt angles around Joy’s law (Hale *et al.* 1919). Due to the spread in tilt angles around Joy’s law, it is quite expected that a few outliers would violate Hale’s law. A study by Stenflo & Kosovichev (2012) estimated about 4% of medium and large sunspots violate Hale’s law. Since this is a small percentage of sunspot numbers, it is not surprising that due to statistical fluctuation, these anti-Hale sunspots appear in some particular cycles compared to the other cycles. Jiang *et al.* (2015) suggested on the basis of their SFT calculations that the appearance of a few large anti-Hale sunspot pairs at a particular cycle can significantly decrease the strength of the polar field at the end of that cycle and this is the reason for the weak polar field at the end of cycle 23 but not cycle 21 or 22.

A large anti-Hale sunspot pair is placed manually by hand in different phases during a cycle in 3D and its effect on the build up of a polar field is studied in the 3D model. The magnetic flux in the anti-Hale sunspot pairs is chosen 25 times the magnetic flux carried by other regular sunspots to make its effect more clearly visible. The tilt angle for the anti-Hale pair is taken as 30° . We consider four different cases to understand how the appearance of an anti-Hale sunspot pair at different emergence latitudes and different phases of the cycle affects the polar field. As sunspots generally appear at high latitudes in the early phase of the cycle and at low latitudes in the late phase, we consider one case by placing the anti-Hale sunspot pair at the high latitude of 40° in the early phase and another case by putting the anti-Hale pair in the late phase at 10° . In the other two cases, the anti-Hale sunspot pair is placed at 40° and 10° latitudes

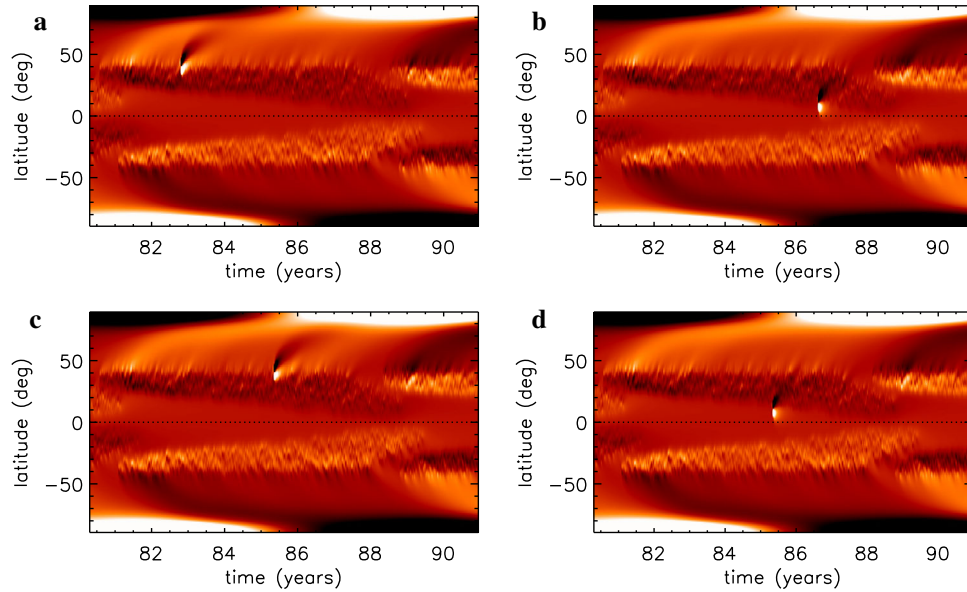


Figure 9. Time–latitude diagram of the radial field on the solar surface with an “anti-Hale” sunspot pair at different latitudes and different phases of the solar cycle. (a) At the early phase of the cycle and at 40° latitude, (b) late phase of the cycle and 10° latitude, (c) middle phase and 40° , and (d) middle phase and 10° latitude. Color scale saturates at ± 15 kG for all four cases. Taken from Hazra *et al.* (2017).

(different case studies) in the middle phase of the cycle. Figure 9 shows the time–latitude plot (“butterfly diagram”) of the radial magnetic field for these four cases. The time evolution of the polar field in these four cases along with a case without an anti-Hale sunspot pair is shown in Figure 10, where the effect of the anti-Hale pair on the polar field is clearly visible.

It is found that an anti-Hale pair near the low-latitude like 10° at any phase of the cycle does not have much effect on the polar field as it is clear from Figure 10. The opposite fluxes from the two sunspots neutralize each other before they reach the poles, which becomes quite apparent from Figure 9(b) and (d). The anti-Hale pair at low latitudes produce a surge behind them but it does not reach the pole. If the anti-Hale pair appears at the high latitudes, its effect is certainly much more pronounced. The surges in these cases reach the poles as we see in Figure 9(a) and (c). When the anti-Hale pair appears at 40° but at the early phase of the cycle, the build up of the polar field is weakened and delayed, but eventually the polar field reaches almost the strength of the polar field that we expect in the absence of the anti-Hale sunspot pair (Figure 10). However, if that pair appears in the middle phase of a cycle, the polar field can be reduced by about 17%. Note that this large reduction arises because the anti-Hale sunspot pair is unrealistically large. In conclusion, an anti-Hale sunspot pair could affect the build up of the polar field—especially if

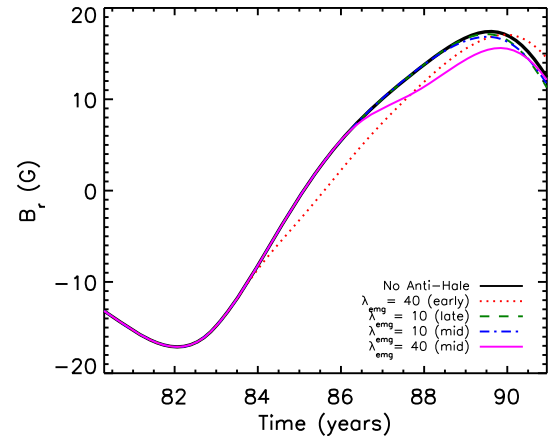


Figure 10. Time evolution of a polar field for one complete solar cycle with the “anti-Hale” sunspot pair at different locations and different times of the cycle taken from Hazra *et al.* (2017). A case of a regular cycle with no anti-Hale sunspot pair is plotted in the solid black line. The red dotted line shows the poloidal field evolution with an anti-Hale pair at 40° latitude at an early phase of the cycle. The green dashed line indicates a poloidal field with an anti-Hale pair at 10° and a late phase. Blue dashed and magenta long dashed lines represent the poloidal field with an anti-Hale pair at the middle of the cycle but at 10° and at 40° latitudes, respectively.

they appear at high latitudes and in the middle phase of a cycle but the effect does not appear to be very dramatic.

On the other hand, recent calculation by Nagy *et al.* (2017) using their $2 \times 2D$ hybrid dynamo model showed that an individual large anti-Hale pair appear as far as 20° from the equator can still have a significant effect on the polar field. The strongest effect on the subsequent cycle occurs when a large pair emerges around cycle maxima but at low latitudes. This finding is also in accordance with Jiang *et al.* (2015) that suggested the weakness of the polar field at the end of cycle 23 was due to the appearance of several anti-Hale sunspot pairs. Since some of the results from the 3D model differ from SFT models due to low-latitude poloidal flux emergence, we believe the difference occurs in the result of the effect of the anti-Hale pair on the polar field in our model and other models is a consequence of the same low-latitude poloidal flux emergence. However, this suggestion merits further detailed study in order to arrive at a firm conclusion.

5. Irregularities of the solar cycle from 3D models

The 3D dynamo model is used to study the irregularity of the solar cycle as well. The plausible causes of irregularity in the solar cycle in the BL dynamo framework include variation in different flux transport mechanisms (convective transport and transport by meridional circulation), differential rotation, and randomness in the BL process. Modeling stochastic variation in convective flows is a challenging problem. It needs the unified understanding of small- and large-scale dynamo action and has been studied by a few groups (e.g., Kitchatinov *et al.* 1994; Karak *et al.* 2014b). The influence of variation in meridional flow is found to be very important to give rise to cycle variability including grand minima and grand maxima (Charbonneau & Dikpati 2000; Karak & Choudhuri 2011, 2013; Hazra *et al.* 2015; Hazra & Choudhuri 2019). From helioseismology, a weak variation in the differential rotation is known to exist (see Chakraborty *et al.* (2009) and references therein for details) but the observed correlation between polar flux at the cycle minimum and the sunspot number of the following cycle suggest that the Ω -effect is largely linear and not a major source of irregularity in the solar cycle (Jiang *et al.* 2007; Wang *et al.* 2009).

Direct observations of the polar field for the last few cycles (Svalgaard *et al.* 2005), as well as some polar

proxies such as polar faculae, polar network index available for the last 100 years, show a clear strong cycle-to-cycle variations in the polar field (Muñoz-Jaramillo *et al.* 2013; Priyal *et al.* 2014; Hazra & Choudhuri 2019). The amount of polar field generation mainly depends on the tilt angle between BMRs, their magnetic fluxes, and the speed of the meridional circulation. Particularly, the scatter of tilt angles around mean, presumably caused by the effect of convective turbulence on the rising flux tubes plays a major role. Recently, Jiang *et al.* (2014a) studied that the tilt angle scatters led to a variation of the polar field by about 30% for cycle 17. Hence, the random scatter in active regions tilt is considered as a possible mechanism to explain the irregularity of the solar cycle (Choudhuri 1992; Charbonneau & Dikpati 2000; Choudhuri *et al.* 2007).

Random scatter in the BMR tilt angles has been studied previously within the context of 2D BL dynamo models (Choudhuri 1992; Charbonneau & Dikpati 2000; Jiang *et al.* 2007; Choudhuri & Karak 2009; Hazra *et al.* 2015), SFT models (Jiang *et al.* 2014b) and in a coupled $2 \times 2D$ BL/SFT model (Lemerle & Charbonneau 2017). For the first time, Karak & Miesch (2017) have considered the random scatter in the tilt angles in the STABLE 3D dynamo model framework. In the STABLE model, the standard Joy's law is used for tilt angle $\delta = \delta_0 \cos \theta$, while implementing the "Spotmaker" algorithm to put bipolar sunspots on the surface of the Sun. To include tilt angle scatter around its mean, a random fluctuating component (δ_f) is added around Joy's law as

$$\delta = \delta_0 \cos \theta + \delta_f. \quad (12)$$

According to observations, Joy's law is a statistical law and there is a considerable scatter around it (Howard 1991; Stenflo & Kosovichev 2012). By analyzing BMRs data measured during 1976–2008, Wang *et al.* (2015) reported that the fluctuation of the tilt (δ_f) roughly follow a Gaussian distribution as given below:

$$f(\delta_f) = \frac{1}{\sigma_\delta \sqrt{2\pi}} \exp[-\delta_f^2 / 2\sigma_\delta^2], \quad (13)$$

where $\sigma_\delta = 15^\circ$.

Also, Karak & Miesch (2017) implemented a tilt angle quenching as the main source of dynamo quenching instead of flux quenching (Equation 11) as used in previous STABLE papers (Miesch & Dikpati 2014; Miesch & Teweldebirhan 2016;

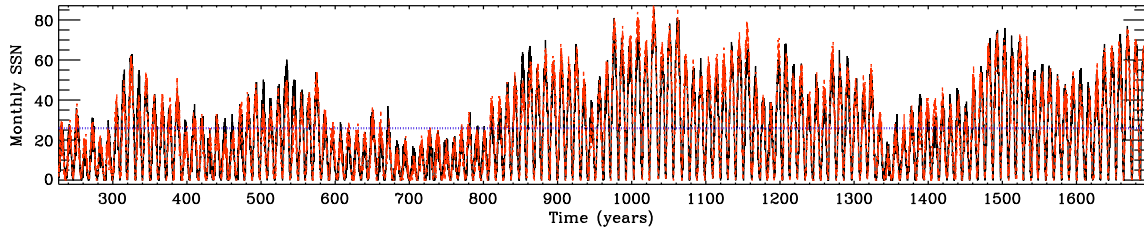


Figure 11. Smoothed (over 3 months) monthly sunspot number is plotted with time. Black and red lines show north and south sunspot numbers, respectively. The dotted line represents the mean of peak sunspot numbers for the last 13 observed solar cycles. This figure is taken from Karak & Miesch (2017).

Hazra *et al.* 2017; Hazra & Miesch 2018). Finally, the tilt used to study the irregularity is given by

$$\delta = \frac{\delta_0 \cos \theta + \delta_f}{1 + B(\theta, \phi, t)/B_q^2}, \quad (14)$$

where $\delta_0 = 35^\circ$ and other terms are as usual. The simulated solar cycle, i.e., the sunspot time series (smoothed over 3 months) is shown in Figure 11. Black and red represent the sunspot numbers in the northern and southern hemispheres, respectively. The cycle-to-cycle variation of the amplitude of the mean polar flux is $\sim 35\%$. This result is in agreement with the study of Jiang *et al.* (2014a), who found a 30% variation in the polar field after introducing tilt angle scatter.

The strength of the magnetic field and the number of bipolar sunspots per cycle has increased in comparison with the case without tilt angle scattering. The variation in the peak SSN in this simulation is 41%, while the observed variation during the period of 1749–2017 in sunspot number data is 32%. Also, the hemispheric asymmetry is observed in the simulated time series of the sunspot numbers. By zooming in Figure 11 carefully, one can clearly find a temporal lag and excess of sunspots numbers between two hemispheres. However, like the real Sun, the STABLE model always tends to correct any hemispheric or temporal asymmetry produced in a cycle and no extended asymmetry is seen. Similar results were also reported using 2D models by Chatterjee & Choudhuri (2006).

In this 3D model, the cycle period has considerable variation around its mean of 10.5 years. In the FTD, the cycle period is largely determined by the speed of the meridional flow. However, while introducing scatter at a tilt angle, the speed of meridional flow is kept constant. Hence, the variation in the cycle period occurred due to the fluctuation and nonlinearities in the BMR emergence. Basically, when the polar field of a cycle becomes stronger due to the tilt fluctuations, spots in the next cycle take a longer time to reverse the previous cycle flux, which makes a longer cycle. On the other

hand, a stronger polar field makes the toroidal field stronger, which leads to more frequent BMR emergence. This effect acts to reverse the polar field quickly and makes the cycle period shorter, although it is inhibited by the tilt angle quenching. Therefore, the tilt angle quenching makes a major role in deciding which effect is prominent and how the period will be varied. Hence, the introduction of an observed tilt angle scatter in the Sun may be sufficient to account for the irregularities observed in the solar cycle.

In 2D BL dynamo models, some of the features of the solar cycle (e.g., Waldmeier effect and correlation between decay rate and amplitude of the next cycle) are not reproduced by introducing randomness in the BL process. So, a variation in the meridional circulation was necessary to explain these features. In the 3D dynamo model, a small correlation arises between the cycle amplitude and the period of the previous cycle ($r = -0.24$) by only including tilt angle scatter, while the observed correlation is $r = -0.67$. Hence, it needs a separate study whether other irregular properties of the solar cycle can be recovered by introducing tilt angle scatter around Joy’s law or we need to introduce fluctuation in the meridional circulation as well.

Figure 11 which includes a tilt angle scatter following a Gaussian distribution with $\sigma_\delta = 15^\circ$ produces very weak and strong cycles and a few Dalton-like extended periods of weak activity (e.g., around 700 years). However, it does not produce any Maunder-like grand minimum or grand maximum. Keeping the possibility in mind that the weaker BMRs might have bigger scatter in their tilt and study of tilt angles does show cycle-to-cycle variations in the tilt angle (Stenflo & Kosovichev 2012; Jiang *et al.* 2014a; Lemerle & Charbonneau 2017), the scatter distribution around mean tilt is doubled. Now $\sigma_\delta = 30^\circ$ is considered instead of 15° . Interestingly, this large fluctuation in the tilt angle does not affect the dynamo operation and dynamo never dies. The cyclic behavior is always maintained. Several episodes of weak

magnetic activity, i.e., maunder-like grand minima arise from this simulation. This simulation produces occasional periods of stronger magnetic activity or grand maxima as well (see Karak & Miesch (2017) for more details).

6. Incorporation of the surface convection

The advantage of extra dimension in the 3D dynamo model allows to explore the implementation of overwhelming observational data available for the Sun. In the STABLE model, Hazra & Miesch (2018) incorporate 3D convective flow fields for the first time in a BL dynamo framework to study their effect on the solar cycle. The dispersal and migration of surface fields are modeled as an effective turbulent diffusion in most of the BL models, but they have incorporated the realistic convective flow to capture the BL process more realistically by exploiting the 3D capabilities of the STABLE model.

The observed line-of-sight velocity on the photosphere measured with the SOHO/MDI Dopplergram instrument is included in the model. 2D maps of the line-of-sight velocity component measured using MDI Dopplergram are shown in Figure 12(a). These velocities in the photosphere are predominantly horizontal and include all information of differential rotation, meridional circulation, other unwanted signals such as convective blueshift, spacecraft motion, and instrumental artifacts. In order to reconstruct the complete 2D convective spectrum of the surface of the Sun, one needs to model the data to get rid of all unwanted information. Hathaway (2012a,b) has devised such a model that subtracted all unwanted above-mentioned signals and computed the

convective power spectrum. After that, a horizontal velocity field is calculated based on that observed spectrum using a series of spherical harmonics with randomized phases. A sample of surface Dopplergram from the simulated horizontal velocity field is shown in Figure 12(b). The power spectrum of the horizontal velocity is also shown in Figure 12(c). The peak around $l = 130$ shows supergranulation.

In order to incorporate the empirical surface velocity field $\mathbf{V}_s(\theta, \phi, t)$ (Figure 12b) into STABLE, a radial structure is specified and the surface field is extrapolated downward into the CZ no deeper than $r = 0.9 R_\odot$. As convection is very vigorous near the surface layers than the deeper CZ, the convective velocity fields are kept confined near the surface layers. Also, these velocities are nonaxisymmetric and they affect the transport and amplification of the magnetic field, which can influence the time evolution of the mean fields.

Note that global convective simulations are fully capable of simulating global-scale convective motions but no global simulation model can accurately capture smaller-scale convective motions near the surface of the Sun such as granulation and supergranulation. This is because it would require both extremely high resolution and some very important physical processes such as non-LTE radiative transfer, ionization, and full compressibility. However, these small-scale convective motions are most important to the breakup and dispersal of BMRs and relevant to the BL process. For this reason, we incorporate convection in a manner that is consistent with the pragmatic approach of kinematic dynamo modeling.

Soon after the implementation of convective flows in the STABLE simulation along with other regular

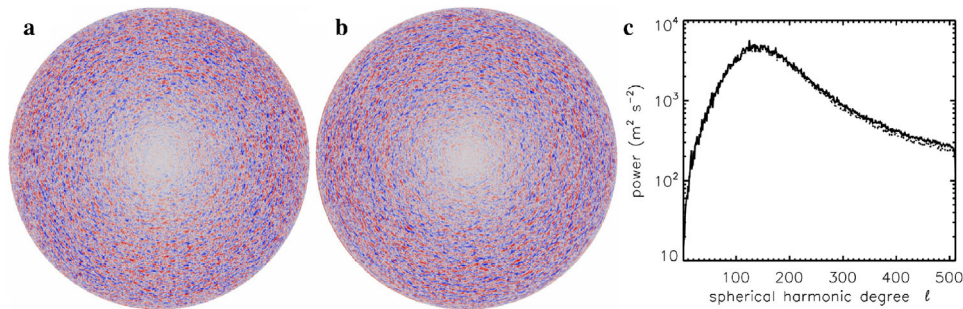


Figure 12. (a) Line-of-sight (Doppler) velocity on the solar photosphere measured using the SOHO/MDI instrument on 4 June 1996. (b) Simulated line-of-sight velocity obtained from the empirical model developed by Hathaway *et al.* (2000) and Hathaway (2012a,b). Hathaway’s models are designed to reproduce the observed horizontal Doppler velocity power spectrum with randomized phases. (c) Horizontal velocity spectra for the convective flow field used here (dotted line) and for Hathaway’s simulated flow field (solid line) at $r = R_\odot$. Small discrepancies at large l arise because we only extract the divergent component. Taken from Hazra & Miesch (2018).

ingredients of the model, it is realized that convective flows do operate as a small-scale dynamo disrupting the operation of the large-scale magnetic cycle. Several approaches are considered to suppress the small-scale dynamo action but the only effective way is to make the convective flows acting only on the radial component of the magnetic field. This also helps to realistically capture the horizontal transport of the vertical magnetic field on the surface layers. Also, note that a background diffusivity $5 \times 10^{11} \text{ cm}^2 \text{ s}^{-1}$ is used to maintain dipolar parity. This background diffusivity helps to suppress small-scale dynamo as well.

The results with an explicit convective transport as the effective transport mechanism of a large-scale magnetic field on the surface are shown in Figure 13. The time evolution of the radial field on the surface (Figure 13a) is comparable with the observed radial field evolution but the presence of mixed polarity near the pole has no counterpart in the observation. The existence of the mixed polarity can be attributed to the tendency for the convective motions to disperse and migrate the BMR field without dissipating them. As a consequence, both polarities are migrated toward the pole and concentrated into strong, alternating bands.

The polar flux plot in Figure 13(b) shows somewhat more variability and a sharper decay near the end of each cycle. This variability occurs due to the existence of mixed polarity fields that cross into the polar regions before they cancel each other. The slower decay phase implies a longer interval of the polar flux

generation by poleward migrating magnetic streams, which persists almost the entire cycle.

The long sustained supply of poloidal flux to the poles throughout most of the cycle has consequences in toroidal field generation. The polar flux behaves as the seed for the next cycle and when it is transported to the base of the CZ by meridional circulation, it promotes sustained toroidal flux generation by Ω -effect, more precisely at the mid-latitudes where the latitudinal shear is strongest. This scenario is evident from Figure 13(c). Throughout most of the cycle, a strong toroidal field persists near $\pm 50^\circ - 60^\circ$. This existence of strong toroidal flux in the mid-latitude also accounts for the distortion of the integrated toroidal flux curve shown in Figure 13(d).

Hazra & Miesch (2018) also address the question of whether the convective transport accurately parameterized by a turbulent diffusion or is it fundamentally nondiffusive? In case it is possible to represent convective transport using a turbulent diffusion then what value of surface diffusivity is optimal? To answer those questions, a few simulations are performed by changing the surface diffusivity value ranging from 1×10^{13} to $8 \times 10^{11} \text{ cm}^2 \text{ s}^{-1}$.

The surface butterfly diagrams for those few cases are shown in Figure 14. Qualitatively, the convective case bears the greatest resemblance to the case with surface diffusivity of $3 \times 10^{11} \text{ cm}^2 \text{ s}^{-1}$. This conclusion is based on the width of the poleward migrating streams, the structure of polar field concentration and

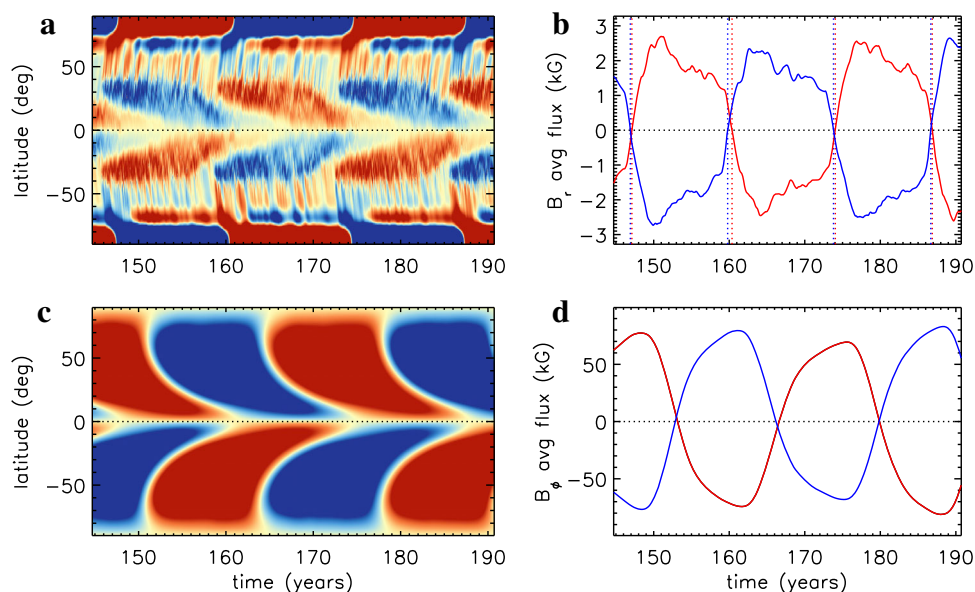


Figure 13. Same as Figure 5 but for the case that includes surface convective flows. The color scale saturates at (a) ± 500 G and (c) ± 100 kG. From Hazra & Miesch (2018).

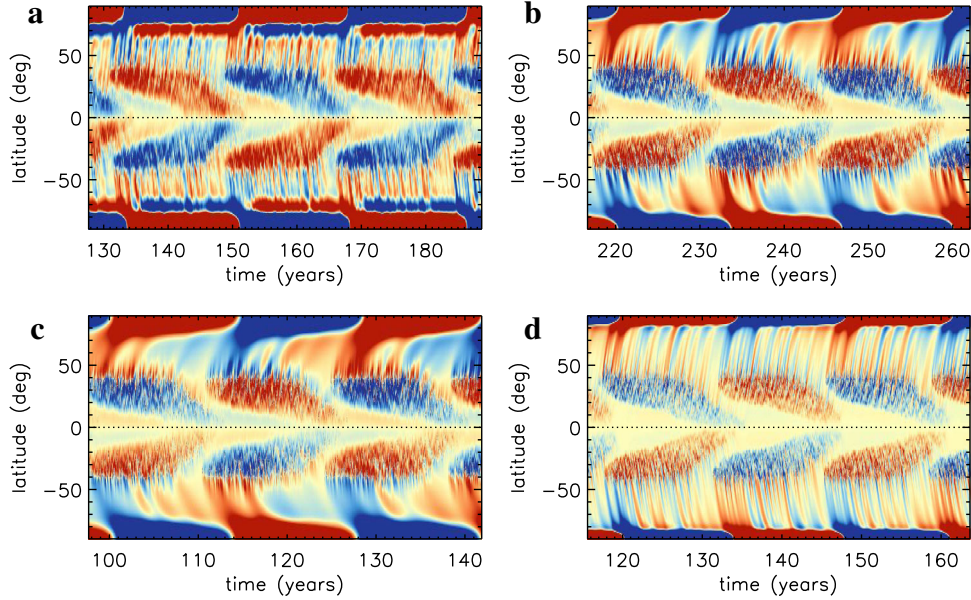


Figure 14. Butterfly diagram of azimuthal averaged B_r , at $r = R_\odot$ for (a) convective case that includes surface convective flows (Br scale = ± 500 G), (b) case with $\eta_{\text{top}} = 3 \times 10^{12} \text{ cm}^2 \text{ s}^{-1}$ (Br scale = ± 200 G), (c) case with $\eta_{\text{top}} = 10^{13} \text{ cm}^2 \text{ s}^{-1}$ (Br scale = ± 30 G), and (d) case with $\eta_{\text{top}} = 8 \times 10^{11} \text{ cm}^2 \text{ s}^{-1}$ (Br scale = ± 800 G). From Hazra & Miesch (2018).

the relative strength of the polar and low-latitude fields, as well as the location of the active latitudes.

Some more quantitative analysis such as calculation of poleward migration speed, dynamo efficiency shows that a turbulent diffusion coefficient of $3 \times 10^{11} \text{ cm}^2 \text{ s}^{-1}$ adequately captures the SFT as in the case with an explicit convective transport but it does not adequately capture the dissipation of magnetic energy (Hazra & Miesch 2018). Approximating convective transport with a turbulent diffusion will have an adverse effect on the dynamo efficiency, which in turn will produce artificially weak mean fields and shorter cycles. However, it is found that replacing turbulent diffusion with convective transport does not improve the fidelity to the butterfly diagrams, giving rise to the mixed polarity fields in the polar regions.

7. Conclusions

Although many alternative solar dynamo models have been proposed, the BL dynamo model has remained the most promising leading framework to explain various properties of the solar cycle so far, because it is firmly based on solar observations and provides a robust mechanism to produce cyclic dynamo activity. However, the BL model is kinematic and solves only axisymmetric mean-field dynamo equations. The

velocity fields are not calculated from the first principle in these models rather they are provided from observations. The basic MHD equations are solved in global MHD models, which have progressed a lot recently (Charbonneau 2014) to reproduce the cyclic activity but they are far away from actual solar parameters. Also, the BL model involves many physical processes (e.g., BL process and magnetic buoyancy) that rather have been parameterized very simplistic ways (Dikpati & Charbonneau 1999; Chatterjee *et al.* 2004; Karak *et al.* 2014b). The 3D kinematic BL dynamo models emerge out as a next-generation dynamo model that holds the promise to model all physical processes more realistically than previous 2D BL models and have the capability to include non-kinematic effects such as back reaction due to the Lorentz force on the flows.

The development of such a kind of 3D model has been started very recently (Yeates & Muñoz-Jaramillo 2013; Miesch & Dikpati 2014; Miesch & Teweldebirhan 2016; Hazra *et al.* 2017; Karak & Miesch 2017; Lemerle & Charbonneau 2017; Kumar *et al.* 2019). The rise of toroidal flux tube due to magnetic buoyancy and subsequent creation of sunspots, which is one of the backbone of BL models, is captured more realistically by including existing knowledge from 3D MHD flux tube emergence simulations as well as observations. Some authors (Yeates & Muñoz-Jaramillo 2013; Kumar *et al.* 2019) have

modeled the buoyant rise of flux tube by applying a radial outward velocity and a vortical velocity simultaneously to a localized part of the toroidal flux tube near the bottom of the CZ assuming that parent flux tubes for sunspots remained connected to its root. Whereas others (e.g., the STABLE model; Miesch & Dikpati 2014; Miesch & Teweldebirhan 2016; Hazra *et al.* 2017) have assumed that the sunspots get quickly disconnected from the parent flux tube and place the sunspots based on the information of toroidal flux near the base of the CZ. In this case, a subsurface structure of sunspots is also specified up to a radius of $0.9R_{\odot}$ from the surface. The latter scenario is preferred as it is argued by Longcope & Choudhuri (2002) and Rempel (2005) that sunspots get quickly disconnected from their parent flux tubes. Recently, Whitbread *et al.* (2019) also argued based on the surface flux evolution that BMRs need to be disconnected from the base of the CZ more rapidly to get better evolution of the surface fields. Our present buoyancy algorithm limits the model in order to explain active longitudes (Mandal *et al.* 2017). However, it has the capability to include TNOs, which are believed to be one of the major drivers of the active longitudes of the Sun (Dikpati & Gilman 2005; Dikpati *et al.* 2018).

The 3D models also study how the solar polar field builds up from the decay of one tilted bipolar sunspot pair and two symmetrically situated sunspot pairs in two hemispheres. It is found that the polar field arising from such sunspot pairs eventually disappears due to the emergence of poloidal flux at low latitudes and subsequent subduction by the meridional flow. These processes are not included in 2D SFT models and the polar field in that models can only be neutralized by diffusion with a field of opposite polarity. So, we conclude that one has to be cautious in interpreting the results of 2D SFT models pertaining to polar fields as SFT models do not capture the dynamics of the polar fields more realistically.

How a few large sunspot pairs violating Hale's law could affect the strength of the polar field is also studied in the 3D models. It is found that anti-Hale pairs do affect solar polar field—especially if they appear at higher latitudes and during the mid-phase of the cycle but the effect is not very dramatic.

Irregularities of the solar cycle are also studied in great detail using 3D models. In contrast to the previous 2D BL dynamo models where randomness arises in the BL mechanism due to the scatter of the tilt angle across Joy's law is included using a stochastic random parameterization as a cause of

irregularity, 3D models actually incorporate the scatter of tilt angle physically in the model. Motivated from the observational findings, a scatter of tilt around Joy's law is modeled using a Gaussian distribution. The cycle irregularities are reproduced quite nicely including grand minima and grand maxima by varying the parameter of the scatter distribution (Karak & Miesch 2017).

The 3D capability of these models is exploited to incorporate high-resolution observed data into the dynamo simulations directly to study their effect on the solar cycle. In the BL dynamo models, the convective flows on the surface of the Sun play a key role in the migration and dispersion of the sunspot fields. Usually, these whole procedures are modeled using an effective turbulent diffusion. This might be because of the unavailability of enough resolution and framework to incorporate convective flows in the simulation. With the newly developed 3D model, realistic convective flows based on solar observation are incorporated in order to improve the fidelity of convective transport. This new study shows that approximating convective transport using a turbulent diffusion underestimates dynamo efficiency producing weaker mean fields and shorter cycles.

3D kinematic dynamo models are capable of producing many attractive features of the solar cycle that were previously not possible by 2D BL dynamo models or 2D SFT models individually. These models incorporate all attractive aspects of both models while being free from the limitation of both. The time evolution of the simulated surface magnetic field can be used to study their effect on the topology of corona and the properties of the solar wind. These models also help us to directly assimilate observed surface data and study their interaction with the solar interior. The direct incorporation of surface data will help us to predict correctly the polar field and hence in predicting the next cycle amplitude. Presently, a snapshot of observed convective flows is only incorporated to study their effect on the surface evolution of the field and effect on the dynamo cycle. In the future, it will be a really important step to assimilate the time-evolving convective flow fields as well as the observed surface magnetograms to constrain the polar field at the end of the cycle. Presently, a small-scale dynamo action after assimilating convective flow fields is encountered, which disrupts large-scale dynamo activity. This small-scale dynamo action can be handled properly if we include Lorentz force feedback to saturate them. Including Lorentz force feedback in the 3D dynamo model would be the next

step to make these models more suitable to study solar and stellar magnetic cycles.

Acknowledgements

The author thanks an anonymous referee for her/his insightful comments which helped to improve the manuscript. The author also would like to thank Prof. Arnab Rai Choudhuri for thoroughly going through the manuscript and giving many useful suggestions that help a lot to improve the review. The author also acknowledges the funding from the European Research Council (ERC) under the European Union's Horizon 2020 research and innovation programme (Grant Agreement No. 817540, ASTROFLOW).

References

- Antia H. M., Basu S., Chitre S. M. 1998, *Mon. Not. R. Astron. Soc.*, 298, 543, <https://doi.org/10.1046/j.1365-8711.1998.01635.x>
- Antia H. M., Basu S. 2000, *Astrophys. J.*, 541, 442, <https://doi.org/10.1086/309421>
- Antia H. M., Basu S., Chitre S. M., 2008, *Astrophys. J.*, 681, 680, <https://doi.org/10.1086/588523>
- Babcock H. W. 1961, *Astrophys. J.*, 133, 572, <https://doi.org/10.1086/147060>
- Baumann I., Schmitt D., Schüssler M., Solanki S. K. 2004, *Astron. Astrophys.*, 426, 1075, <https://doi.org/10.1051/0004-6361:20048024>
- Baumann I., Schmitt D., Schüssler M. 2006, *Astron. Astrophys.*, 446, 307, <https://doi.org/10.1051/0004-6361:20053488>
- Berdugina S. V. 2005, *Living Rev. Solar Phys.*, 2, 8, <https://doi.org/10.12942/lrsp-2005-8>
- Chakraborty S., Choudhuri A. R., Chatterjee P. 2009, *Phys. Rev. Lett.*, 102, 041102, <https://doi.org/10.1103/PhysRevLett.102.041102>
- Charbonneau P., Dikpati M. 2000, *Astrophys. J.*, 543, 1027, <https://doi.org/10.1086/317142>
- Charbonneau P. 2014, *Ann. Rev. Astron. Astrophys.*, 52, 251, <https://doi.org/10.1146/annurev-astro-081913-040012>
- Chatterjee P., Nandy D., Choudhuri A. R., 2004, *Astron. Astrophys.*, 427, 1019, <https://doi.org/10.1051/0004-6361:20041199>
- Chatterjee P., Choudhuri A. R., 2006, *Solar Phys.*, 239, 29, <https://doi.org/10.1007/s11207-006-0201-6>
- Choudhuri A. R. 1992, *Astron. Astrophys.*, 253, 277
- Choudhuri A. R., Schüssler M., Dikpati M. 1995, *Astron. Astrophys.*, 303, L29
- Choudhuri A. R. 1998, *The Physics of Fluids and Plasmas: An Introduction for Astrophysicists*. Cambridge University Press, Cambridge
- Choudhuri A. R., Dikpati M. 1999, *Solar Phys.*, 184, 61, <https://doi.org/10.1023/A:1005092601436>
- Choudhuri A. R., Chatterjee P., Jiang J. 2007, *Phys. Rev. Lett.*, 98, 131103, <https://doi.org/10.1103/PhysRevLett.98.131103>
- Choudhuri A. R., Karak B. B. 2009, *Res. Astron. Astrophys.*, 9, 953, <https://doi.org/10.1088/1674-4527/9/9/001>
- Choudhuri A. R., Hazra G. 2016, *Adv. Space Res.* 58, 1560, <https://doi.org/10.1016/j.asr.2016.03.015>
- Dasi-Espuig M., Solanki S. K., Krivova N. A., Cameron R., Peñuela T. 2010, *Astron. Astrophys.*, 518, A7, <https://doi.org/10.1051/0004-6361/201014301>
- Dikpati M., Choudhuri A. R. 1994, *Astron. Astrophys.*, 291, 975
- Dikpati M., Choudhuri A. R. 1995, *Solar Phys.*, 161, 9, <https://doi.org/10.1007/BF00732081>
- Dikpati M., Charbonneau P. 1999, *Astrophys. J.*, 518, 508, <https://doi.org/10.1086/307269>
- Dikpati M., Gilman P. A. 2005, *Astrophys. J. Lett.*, 635, L193, <https://doi.org/10.1086/499626>
- Dikpati M., McIntosh S. W., Bothun G., *et al.* 2018, *Astrophys. J.*, 853, 144, <https://doi.org/10.3847/1538-4357/aaa70d>
- Dikpati M., McIntosh S. W. 2020, *Space Weather*, 18, e02109, <https://doi.org/10.1029/2019SW002109>
- D'Silva S., Choudhuri A. R. 1993, *Astron. Astrophys.*, 272, 621
- Durney B. R. 1995, *Solar Phys.*, 160, 213, <https://doi.org/10.1007/BF00732805>
- Durney B. R. 1997, *Astrophys. J.*, 486, 1065
- Gizon L., Cameron R. H., Pourabdian M., *et al.* 2020, *Science*, 368, 1469, <https://doi.org/10.1126/science.aaz7119>
- Gopalswamy N., Yashiro S., Krucker S., Stenborg G., Howard R. A. 2004, *J. Geophys. Res. (Space Phys.)*, 109, A12105, <https://doi.org/10.1029/2004JA010602>
- Hale G. E., 1909 *Pub. Astron. Soc. Pac.*, 21, 205, <https://doi.org/10.1086/121926>
- Hale G. E., Ellerman F., Nicholson S. B., Joy A. H. 1919, *Astrophys. J.*, 49, 153, <https://doi.org/10.1086/142452>
- Hathaway D. H. 2012a, *Astrophys. J. Lett.*, 749, L13, <https://doi.org/10.1088/2041-8205/749/1/L13>
- Hathaway D. H. 2012b, *Astrophys. J.*, 760, 84, <https://doi.org/10.1088/0004-637X/760/1/84>
- Hazra G., Karak B. B., Choudhuri A. R. 2014, *Astrophys. J.*, 782, 93, <https://doi.org/10.1088/0004-637X/782/2/93>
- Hazra G., Karak B. B., Banerjee D., Choudhuri A. R. 2015, *Solar Phys.*, 290, 1851, <https://doi.org/10.1007/s11207-015-0718-8>
- Hazra G., Choudhuri A. R., Miesch M. S. 2017, *Astrophys. J.*, 835, 39, <https://doi.org/10.3847/1538-4357/835/1/39>
- Hazra G., Miesch M. S., 2018, *Astrophys. J.*, 864, 110, <https://doi.org/10.3847/1538-4357/aad556>

- Hazra G., Choudhuri A. R. 2019, *Astrophys. J.*, 880, 113, <https://doi.org/10.3847/1538-4357/ab2718>
- Hazra G., Jiang J., Karak B. B., Kitchatinov L. 2019, *Astrophys. J.*, 884, 35, <https://doi.org/10.3847/1538-4357/ab4128>
- Hazra G., Vidotto A. A., D'Angelo C. V. 2020, *Mon. Not. R. Astron. Soc.*, 496, 4017, <https://doi.org/10.1093/mnras/staa1815>
- Howard R. F. 1991, *Solar Phys.*, 136, 251, <https://doi.org/10.1007/BF00146534>
- Jiang J., Chatterjee P., Choudhuri A. R. 2007, *Mon. Not. R. Astron. Soc.*, 381, 1527, <https://doi.org/10.1111/j.1365-2966.2007.12267.x>
- Jiang J., Cameron R. H., Schüssler M. 2014a, *Astrophys. J.*, 791, 5, <https://doi.org/10.1088/0004-637X/791/1/5>
- Jiang J., Hathaway D. H., Cameron R. H., Solanki S. K., Gizon L., Upton L. 2014b, *Space Sci. Rev.*, 186, 491, <https://doi.org/10.1007/s11214-014-0083-1>
- Jiang J., Cameron R. H., Schüssler M. 2015, *Astrophys. J. Lett.*, 808, L28, <https://doi.org/10.1088/2041-8205/808/1/L28>
- Karak B. B., Choudhuri A. R. 2011, *Mon. Not. R. Astron. Soc.*, 410, 1503, <https://doi.org/10.1111/j.1365-2966.2010.17531.x>
- Karak B. B., Choudhuri A. R. 2013, *Res. Astron. Astrophys.*, 13, 1339, <https://doi.org/10.1088/1674-4527/13/11/005>
- Karak B. B., Kitchatinov L. L., Choudhuri A. R., 2014a, *Astrophys. J.*, 791, 59, <https://doi.org/10.1088/0004-637X/791/1/59>
- Karak B. B., Rheinhardt M., Brandenburg A., Käpylä P. J., Käpylä M. J. 2014b, *Astrophys. J.*, 795, 16, <https://doi.org/10.1088/0004-637X/795/1/16>
- Karak B. B., Cameron R. 2016, *Astrophys. J.*, 832, 94, <https://doi.org/10.3847/0004-637X/832/1/94>
- Karak B. B., Miesch M. 2017, *Astrophys. J.*, 847, 69, <https://doi.org/10.3847/1538-4357/aa8636>
- Karak B. B., Miesch M. 2018, *Astrophys. J. Lett.*, 860, L26, <https://doi.org/10.3847/2041-8213/aaca97>
- Kitchatinov L. L., Pipin V. V., Ruediger G. 1994, *Astron. Nachrichten*, 315, 157, <https://doi.org/10.1002/asna.2103150205>
- Kitchatinov L. L., Olemskoy S. V. 2011, *Astron. Lett.*, 37, 656, <https://doi.org/10.1134/S0320010811080031>
- Kumar R., Jouve L., Nandy D. 2019, *Astron. Astrophys.*, 623, A54, <https://doi.org/10.1051/0004-6361/201834705>
- Leighton R. B. 1969, *Astrophys. J.*, 156, 1, <https://doi.org/10.1086/149943>
- Lemerle A., Charbonneau P., 2017, *Astrophys. J.*, 834, 133, <https://doi.org/10.3847/1538-4357/834/2/133>
- Longcope D., Choudhuri A. R. 2002, *Solar Phys.*, 205, 63, <https://doi.org/10.1023/A:1013896013842>
- Mandal S., Chatterjee S., Banerjee D. 2017, *Astrophys. J.*, 835, 62, <https://doi.org/10.3847/1538-4357/835/1/62>
- Manoharan P. K., Gopalswamy N., Yashiro S., *et al.* 2004, *J. Geophys. Res. (Space Phys.)*, 109, A06109, <https://doi.org/10.1029/2003JA010300>
- McIntosh S. W., Leamon R. J., Krista L. D., *et al.* 2015, *Nat. Commun.*, 6, 6491, <https://doi.org/10.1038/ncomms7491>
- Miesch M. S., Dikpati M. 2014, *Astrophys. J. Lett.*, 785, L8, <https://doi.org/10.1088/2041-8205/785/1/L8>
- Miesch, M. S., Teweldebirhan K. 2016. *Adv. Space Res.*, 58, 1571
- Muñoz-Jaramillo A., Nandy D., Martens P. C. H., Yeates A. R. 2010, *Astrophys. J. Lett.*, 720, L20, <https://doi.org/10.1088/2041-8205/720/1/L20>
- Muñoz-Jaramillo A., Dasi-Espuig M., Balmaceda L. A., DeLuca E. E. 2013, *Astrophys. J. Lett.*, 767, L25, <https://doi.org/10.1088/2041-8205/767/2/L25>
- Nagy M., Lemerle A., Labonville F., Petrovay K., Charbonneau P. 2017, *Solar Phys.*, 292, 167, <https://doi.org/10.1007/s11207-017-1194-0>
- Parker E. N. 1955, *Astrophys. J.*, 122, 293, <https://doi.org/10.1086/146087>.
- Passos D., Charbonneau P., Miesch M. 2015, *Astrophys. J. Lett.*, 800, L18, <https://doi.org/10.1088/2041-8205/800/1/L18>
- Priyal M., Banerjee D., Karak B. B., *et al.* 2014, *Astrophys. J. Lett.*, 793, L4, <https://doi.org/10.1088/2041-8205/793/1/L4>
- Rempel M. 2005, *Astrophys. J.*, 622, 1320, <https://doi.org/10.1086/428282>
- Robbrecht E., Berghmans D., Van der Linden R. A. M. 2009, *Astrophys. J.*, 691, 1222, <https://doi.org/10.1088/0004-637X/691/2/1222>
- Schou J., Antia H. M., Basu S., *et al.* 1998, *Astrophys. J.*, 505, 390, <https://doi.org/10.1086/306146>
- Stenflo J. O., Kosovichev A. G. 2012, *Astrophys. J.*, 745, 129, <https://doi.org/10.1088/0004-637X/745/2/129>
- Svalgaard L., Cliver E. W., Kamide Y. 2005, *Geophys. Res. Lett.*, 32, L01104, <https://doi.org/10.1029/2004GL021664>
- Thompson M. J., Toomre J., Anderson E. R., *et al.* 1996, *Science*, 272, 1300, <https://doi.org/10.1126/science.272.5266.1300>
- Tokumaru M., Kojima M., Fujiki K. 2010, *J. Geophys. Res. (Space Phys.)*, 115, A04102, <https://doi.org/10.1029/2009JA014628>
- Usoskin I. G., Berdyugina S. V., Poutanen J. 2005, *Astron. Astrophys.*, 441, 347, <https://doi.org/10.1051/0004-6361/20053201>
- Wang Y.-M., Nash A. G., Sheeley Jr. N. R. 1989a, *Science*, 245, 712, <https://doi.org/10.1126/science.245.4919.712>
- Wang Y. M., Nash Jr. A. G., Sheeley, N. R. 1989b, *Astrophys. J.*, 347, 529, <https://doi.org/10.1086/168143>
- Wang Y. M., Robbrecht Jr. E., Sheeley, N. R. 2009, *Astrophys. J.*, 707, 1372, <https://doi.org/10.1088/0004-637X/707/2/1372>

- Wang Y.-M., Colaninno R. C., Baranyi T., Li J. 2015, *Astrophys. J.*, 798, 50, <https://doi.org/10.1088/0004-637X/798/1/50>
- Weber M. A., Fan Y., Miesch M. S., 2011, *Astrophys. J.*, 741, 11, <https://doi.org/10.1088/0004-637X/741/1/11>
- Whitbread T., Yeates A. R., Muñoz-Jaramillo A. 2019, *Astron. Astrophys.*, 627, A168, <https://doi.org/10.1051/0004-6361/201935986>.
- Winter L. M., Pernak R. L., Balasubramaniam K. S. 2016, *Solar Phys.*, 291, 3011, <https://doi.org/10.1007/s11207-016-0901-6>
- Wu C. J., Krivova N. A., Solanki S. K., Usoskin I. G. 2018, *Astron. Astrophys.*, 620, A120, <https://doi.org/10.1051/0004-6361/201832956>
- Yashiro S., Gopalswamy N., Michalek G., *et al.* 2004, *J. Geophys. Res. (Space Phys.)*, 109, A07105, <https://doi.org/10.1029/2003JA010282>
- Yeates A. R., Muñoz-Jaramillo A. 2013, *Mon. Not. R. Astron. Soc.*, 436, 3366, <https://doi.org/10.1093/mnras/stt1818>
- Yoshimura H. 1975, *Astrophys. J.*, 201, 740, <https://doi.org/10.1086/153940>